

**FEDSM2003-45395**

## **A COMPUTATIONAL METHODOLOGY FOR LARGE-EDDY SIMULATION OF TIP-CLEARANCE FLOWS**

Donghyun You,<sup>1</sup> Rajat Mittal,<sup>2</sup> Meng Wang<sup>1</sup> and Parviz Moin<sup>1</sup>

<sup>1</sup>Center for Turbulence Research, Stanford University, Stanford, CA 94305

<sup>2</sup>Department of Mechanical and Aerospace Engineering, The George Washington University, Washington, DC 20052

### **ABSTRACT**

A large-eddy simulation (LES) solver which combines an immersed-boundary technique with a curvilinear structured grid has been developed to study the temporal and spatial dynamics of an incompressible rotor tip-clearance flow. The overall objective of these simulations is to determine the underlying mechanisms for low-pressure fluctuations downstream of the rotor near the endwall. Salient features of the numerical methodology, including the mesh topology, the immersed boundary method, the treatment of numerical instability for non-dissipative schemes on highly skewed meshes, and the parallelization of the code for shared memory platforms are discussed. The computational approach is shown to be capable of capturing the evolution of the highly complicated flowfield characterized by the interaction of distinct blade-associated vortical structures with the turbulent endwall boundary layer. Simulation results are compared with experiments and qualitative as well as quantitative agreement is observed.

### **INTRODUCTION**

The existence of tip-clearance is a major source of performance deterioration for axial turbomachines. In a transonic compressor, the interaction between the passage shock and the tip-leakage vortex is implicated in degradation of efficiency as well as noise generation [1]. Also, the tip-clearance is responsible for a significant portion of performance losses in turbines and the blade-tip is known to be susceptible to damage from excessive thermal loading [2]. These issues have motivated a number of experimental and computational investigations of the tip-leakage flow configuration [1-10].

For liquid handling systems like axial pumps and ducted propellers (Fig. 1), the rotor tip-clearance is also considered to be the cause for low-pressure fluctuations downstream of the rotor in the vicinity of the endwall. Experimental studies of the incompressible rotor tip-clearance flow [3-5] indicate that the low pressure fluctuations can result from the turbulence associated with the tip-leakage vortex. Pressure measurements

of Kang and Hirsch [6, 7] show that the tip-leakage vortex dominates much of the endwall flow region. The formation and size of the tip-leakage vortex is also known to be highly dependent on the size of the tip-gap [5]. An incompressible compressor cascade studied by Storer and Cumpsty [8] with different tip-gap sizes showed that for smaller tip gaps (less than 1% of the chord), there was no clear indication of a tip-leakage vortex, while for tip gaps greater than 2% of the chord, a tip-leakage vortex formed on the suction side of the blade.

Recently, Muthanna [9] and Wang [10] have made detailed measurements of the flowfield downstream of rotor blades in a low-speed linear compressor cascade employing stationary and moving endwalls. The objective in this study was to examine the effect of the relative motion between the rotor blade-tip and the casing on the tip-leakage flow. The results showed significant differences in the formation and the evolution of tip-leakage flows between the moving and stationary endwall experiments.

Although these and other experiments have provided useful information regarding the rotor tip-clearance flow, significant gaps still exist in our knowledge of the dynamics of the tip-clearance flow as well as the resulting cavitation-inducing low-pressure fluctuations. This is primarily due to the difficulty in making detailed measurements in the vicinity of a moving blade or endwall casing as well as in simultaneously measuring velocity, vorticity and pressure. To understand the mechanisms for cavitation, it is necessary to study the detailed turbulence dynamics in the rotor blade wake and the clearance region between the rotor tip and the endwall casing. Given the highly unsteady nature of the flow and the need to resolve a range of important flow structures, computational approaches based on the Reynolds-averaged Navier-Stokes (RANS) equations are not ideally suited for a detailed analysis of this flow. In addition to this, time-accurate simulations of the tip-clearance configurations have been difficult due to the geometric complexity, which often leads to highly skewed, large-aspect-ratio meshes and very small computational time steps.

In the present study we have used LES to simulate and study this flow. LES is especially suited for this type of flow

since the Reynolds numbers are relatively low [ $O(10^5)$ ] which brings these flows within the reach of this modeling approach and furthermore, LES provides detailed spatial and temporal information regarding a wide range of turbulence scales which is precisely what is needed to gain better insight into the flow physics of this configuration.

The LES flow solver that has been developed for these simulations is fully three-dimensional with no statistically homogeneous directions and employs an immersed-boundary method in combination with a structured, curvilinear mesh topology to facilitate boundary condition application in the tip-gap region. This flow solver is used to simulate the experimental configuration of Wang [10] for a linear compressor cascade with a moving endwall. It should be pointed out that despite the seeming simplicity of the chosen configuration, these are some of the most complex and ambitious large-eddy simulations attempted to date. At the outset, it was estimated that each simulation would require a grid with  $O(10^7)$  points and  $O(10^5)$  time steps which would translate to  $O(10^5)$  single-processor CPU hours on SGI Origin 3800 per simulation. In addition, each simulation was estimated to require over 10GB of memory and over a Terabyte of disk space. Therefore, these simulations were deemed feasible only on large-scale parallel computers. In this paper, we describe in detail the numerical and computational aspects of the LES flow solver developed for the tip-clearance flow and this is followed by a discussion of results from the simulation.

## NOMENCLATURE

$C$	= chord length
$C_a$	= axial chord length
$c$	= Smagorinsky coefficient
$f_i$	= body force
$p$	= pressure
$Re$	= Reynolds number
$S_{ij}$	= Strain rate tensor
$T$	= averaging time scale
$t$	= time
$U$	= inflow freestream velocity
$u_i$	= $x_i$ component of velocity
$u$	= streamwise velocity
$v$	= cross-stream velocity
$w$	= vertical velocity
$x_i$	= Cartesian coordinate
$x$	= streamwise direction
$y$	= cross-stream direction
$z$	= vertical direction
$\Delta$	= grid spacing
$\bar{\rho}$	= density
$\tau_{ij}$	= subgrid-scale stress tensor

## Superscripts and Subscripts

$\bar{\phantom{x}}$	= filtered quantity
$\tilde{\phantom{x}}$	= test-filtered quantity
$^+\phantom{x}$	= quantity in wall-unit

## NUMERICAL METHODOLOGY

**Numerical Method.** The numerical method is based upon the generalized-coordinate Navier-Stokes solver originally developed by Choi et al. [11], with significant enhancements to treat the special difficulties associated with the tip-clearance flow. The spatially filtered Navier-Stokes equations for resolved scales in LES are as follows:

$$\frac{\partial \bar{u}_i}{\partial t} + \frac{\partial}{\partial x_j} \bar{u}_i \bar{u}_j = -\frac{\partial \bar{p}}{\partial x_i} + \frac{1}{Re} \frac{\partial}{\partial x_j} \frac{\partial \bar{u}_i}{\partial x_j} - \frac{\partial \tau_{ij}}{\partial x_j}, \quad (1)$$

$$\frac{\partial \bar{u}_i}{\partial x_i} = 0, \quad (2)$$

where  $\tau_{ij}$  is the subgrid scale (SGS) stress tensor. All the coordinate variables, velocity components, and pressure are nondimensionalized by the total chord  $C$ , the inflow freestream velocity  $U$ , and  $\sqrt{U^2}$ , respectively. The time is normalized by  $C/U$ . The governing equations (1) and (2) are rewritten in a conservative form in generalized coordinates. The dependent variables in the transformed Navier-Stokes equations are volume fluxes across the faces of the cells, which are equivalent to using the contravariant velocity components on a staggered grid multiplied by the Jacobian of the coordinate transformation. With this choice of variables, the discretized mass conservation can be easily satisfied. The terms in the transformed equations are described in detail in Ref. [11]. The key feature of the numerical method is the use of a non-dissipative, central-difference spatial discretization scheme which has been demonstrated to be crucial for retaining the accuracy and predictive capability of the LES approach [12, 13].

The SGS stress tensor  $\tau_{ij}$  is modeled by a Smagorinsky type eddy-viscosity model:

$$\tau_{ij} = \frac{1}{3} \tau_{kk} \delta_{ij} = 2c \bar{\rho}^2 |\bar{S}| \bar{S}_{ij}, \quad (3)$$

Given that the tip-clearance flow is fully three-dimensional with no homogeneous directions, the Lagrangian dynamic SGS model [14] is employed in order to compute Smagorinsky coefficient  $c$ . The Lagrangian dynamic model averages the model coefficient along the flow pathlines and therefore does not require a homogeneous direction [15]. The equation for computing the coefficient is:

$$c^2(\mathbf{x}, t) = \frac{\tau_{LM}}{\tau_{MM}}, \quad (4)$$

where

$$\tau_{LM} = \frac{1}{T} \int_{\Delta} L_{ij} M_{ij}(\mathbf{z}(t), t) e^{\Delta(\mathbf{x}(t)-\mathbf{z}(t))/T} dt \quad (5)$$

$$\tau_{MM} = \frac{1}{T} \int_{\Delta} M_{ij} M_{ij}(\mathbf{z}(t), t) e^{\Delta(\mathbf{x}(t)-\mathbf{z}(t))/T} dt \quad (6)$$

$T$  is an averaging time scale and the identities  $L_{ij}$ ,  $M_{ij}$  and  $\mathbf{z}$  are defined with velocity components  $u_i$ , grid spacing  $\Delta$  and strain rate tensor  $S_{ij}$  as following:

$$L_{ij} = \frac{1}{\Delta} \frac{\partial u_i}{\partial x_j} - \frac{1}{\Delta} \frac{\partial u_j}{\partial x_i}, \quad (7)$$

$$M_{ij} = 2 \left[ \frac{1}{S} \frac{\partial}{\partial x_j} \frac{\partial}{\partial x_i} \right] \quad (8)$$

$$\mathbf{z}(t) = \mathbf{x} \int_0^t \bar{\mathbf{u}}(\mathbf{z}(t'), t') dt' \quad (9)$$

The integration method used to solve the transformed governing equations is based on a fully-implicit fractional step method which avoids the severe time-step restriction that would occur in the tip-clearance region. All terms including cross-derivative diffusion terms are advanced using the Crank-Nicolson method in time and are discretized by the second-order central-difference in space. A Newton iterative method is used to solve the discretized nonlinear equations.

Since the solution of the Poisson solver is the most expensive part of computation in this fully three-dimensional flow, it is crucial to employ a method which exhibits fast convergence as well as high parallel efficiency. In the current simulations, we employ a highly efficient multigrid procedure, which is also appropriate for parallelization. By experimenting with various solution methods, we have found that a combination of the Gauss-Seidel multigrid method in the streamwise and spanwise directions and a tridiagonal solver in the periodic direction provides the most efficient solution procedure.

The entire code has been parallelized using message passing directives (OpenMP) for shared memory platforms like SGI Origin 2000/3800 and Compaq GS320. Significant effort has been put into optimizing the parallel performance by utilizing cache-management strategies and minimizing data dependency. Figure 2 shows the scaleup achieved on a 256 × 256 × 256 grid with up to 64 processors of SGI Origin 2000. The scaleup factor ( $S$ ) is defined by the ratio of the wallclock time ( $T_i$ ) from a unit CPU to the wallclock time ( $T_N$ ) achieved using  $N$ -CPU's ( $S = T_1/T_N$ ). The code achieves close to linear scaleup thereby indicating nearly optimal parallel efficiency.

**Flow Configuration.** The flow configuration is schematically shown in Fig. 3 along with coordinate definition. The present study is focused on a linear cascade matching the experimental setup of Wang [10]. The rotor blade has a small tip-clearance with the endwall as shown in Fig. 4. The computational domain is of size  $L_x \times L_y \times L_z = 1.6C \times 0.929C \times 0.5C$ , where  $C$  is the chord length.

The full computational domain and grid distribution in a plane perpendicular to the blade (parallel to the endwall) is shown in Fig. 5(a). The third direction is Cartesian with non-uniform grid distributions (see Fig. 4). The rotor is placed near the inflow station so as to leave an adequate region for analysis of downstream turbulence. The simulation is performed in a frame of reference attached to the rotor, with a moving endwall mimicking the moving belt in the experiment [10].

Periodic boundary conditions used along the  $y$ -direction allow us to mimic the flow in the interior of the cascade. The  $y$ -direction domain size  $L_y = 0.929C$  as in the experiment. A simplification is made by terminating the blade-span to one-half chord length and imposing inviscid flow boundary conditions on that boundary:

$$\frac{\partial u}{\partial z} = \frac{\partial v}{\partial z} = w = 0, \text{ at } z = 0.5C. \quad (10)$$

This is justified by observing that the root vortex at the hub does not play any significant role in the convected low-pressure fluctuations which are found near the endwalls. In Wang's experiment [10], the tip-leakage vortex extends to about one-quarter of a chord length from the endwall. The inflow turbulent boundary layer data is provided using the method of Lund et al. [16], modified to account for the fact that the mean flow direction is not perpendicular to the inflow/outflow plane.

No-slip boundary conditions are applied along the rotor blade and moving endwall:

$$u = w = 0, v = V_{belt}, \text{ at } z = 0, \quad (11)$$

and the convective boundary condition,

$$\frac{\partial u_i}{\partial t} + U_c \frac{\partial u_i}{\partial x_1} = 0, \quad (12)$$

is applied at the exit boundary, where the convection speed  $U_c$  is set equal to the mean streamwise velocity integrated across the exit plane.

The blade has a relatively high stagger-angle of about 57 degree (see Fig. 5). This high stagger angle necessitates a highly skewed mesh and requires fine control of mesh parameters such as the grid stretching ratio and cell aspect ratio. The size of the tip-clearance is 1.6% of the total chord, and the blade pitch is 0.9 chord. The Reynolds number of this flow is 400,000 based on the chord and inflow freestream velocity, and the inflow turbulent boundary layer has a Reynolds number of 780 based on the momentum thickness.

### Mesh Topology and Immersed Boundary Method.

The presence of the tip-clearance region between the rotor tip and the endwall poses a considerable challenge for the grid topology and resolution and this factor has in fact been a major obstacle to the accurate prediction of this flow. Commonly used mesh topologies are the multi-zone mesh, which combines H- and O-type meshes (e.g. Ref. [1-2]), and the embedded H-type mesh (e.g., Ref. [17]). However, the zonal mesh and the embedded H-mesh have significant drawbacks for use in LES. This is so because the interpolation procedures in multi-zone meshes and the convergence of the longitudinal grid lines in the leading and trailing edge regions in embedded H-type meshes leads to high aspect and stretching ratios, which are inappropriate for non-dissipative, energy-conservative numerical schemes [13, 18, 19].

In recent years the immersed boundary method [20] has emerged as a flexible and efficient tool for treating boundary conditions in complex geometries or even in moving geometries. With this approach, the simulations can be carried out on a simple grid (see Figs. 5(b) and (c) for grid assignments near leading and trailing edges in tip-clearance configuration), and boundary conditions are assigned by applying body forces to the momentum equations to mimic the effect of the boundary:

$$f_i^n = \frac{(\bar{u}_{i(desired)} - \bar{u}_i)^n}{\Delta t} + \frac{\partial}{\partial x_j} (\bar{u}_i \bar{u}_j)^n + \frac{\partial \bar{p}^n}{\partial x_i} \left[ \frac{1}{\text{Re}} \frac{\partial}{\partial x_j} \frac{\partial \bar{u}_i^n}{\partial x_j} + \frac{\partial \bar{\Gamma}_j^n}{\partial x_j} \right]. \quad (13)$$

Figure. 6 shows an example of body force assignment. Applying a linear or bilinear interpolation technique to point C of outside velocity,  $\bar{u}_{k,l+1}$ , and to B of boundary velocity (e.g., zero in Fig. 6), the velocity inside of the boundary at A,  $\bar{u}_{k,l}$  is estimated. Using this estimation and Eq. (13) the desired body force at the point is obtained.

The implementation of this immersed-boundary method has been validated in a number of canonical flow problems. For example, table 1 shows a comparison among the present simulation with immersed boundary method, simulation on body-fitted mesh [21], and experiment [22] in the case of flow over a circular cylinder at low Reynolds numbers.

	Re	$C_D$	$C_L'$	St
Present	60	1.40	0.134	0.136
	100	1.33	0.330	0.166
	160	1.31	0.560	0.188
Park <i>et al.</i> [21]	60	1.39	0.134	0.136
	100	1.33	0.320	0.165
	160	1.32	0.550	0.188
Williamson [22]	100			0.164

Table 1 Comparison of the results from the present immersed boundary method with 321x321 mesh, body-fitted mesh simulation with 641x241 mesh [21], and experiment [22].  $C_D$ ,  $C_L'$  and St are drag coefficient, lift coefficient and Strouhal number, respectively.

Although a Cartesian mesh is preferred due to the simplicity and efficiency of the solver, the need to resolve the thin turbulent boundary layers at high Reynolds numbers can lead to a very large mesh size if a Cartesian mesh is used. To overcome the above difficulty, a novel approach, which combines the immersed boundary technique with a structured grid in generalized curvilinear coordinates is employed to treat the tip-gap region. The advantage of using a curvilinear mesh is that we can generate grid lines almost parallel to the blade surface, as demonstrated in Fig. 5. This ensures an adequate resolution of the boundary layers, and allows periodic boundary conditions to be applied on the curved upper and lower boundaries. The immersed boundary method when used with the curvilinear mesh, obviates a complex mesh topology and allows us to use a simple single-block mesh.

**Grid Skewness and Numerical Stability.** The large blade angle coupled with the need to have a periodic grid in the crosstream direction leads to a mesh that is highly skewed over the blade surface. For such mesh topologies, non-dissipative schemes such as the one employed here, tend to exhibit highly enhanced dispersive error, which can affect the quality of computed results and sometimes even lead to numerical instability. This was our experience with preliminary

simulation in this configuration as well as simulation of flow through a low-pressure turbine [18, 23].

It is well known that numerical instability for non-dissipative schemes is often caused by the high local Peclet numbers, large mesh stretching ratio, large mesh aspect ratio and mesh unsmoothness. Among these, the effect of mesh skewness is the least understood. In the current study extensive tests have been carried out in order to examine various aspects related to grid skewness. A test of various formulations of the non-linear convection terms indicated that with a highly skewed mesh, the divergence and skew-symmetric forms lead to superior stability characteristics as compared to the rotational form [18].

In addition to this, truncation error analysis indicates that central difference discretization of the Navier-Stokes equations on a highly skewed and stretched mesh leads to spurious negative diffusion terms in the modified equation. Since grid skewness is controlled by the geometry of the blade, the only means of controlling the negative diffusion is through careful control of the grid stretching ratio. In the current simulation, we therefore use meshes where the grid stretching ratio in both directions is kept small. This leads to an increase in the mesh size and consequently the computational resources.

It should be pointed out that grid skewness related problems are usually not observed in conjunction with numerical schemes that employ numerical dissipation (either through upwinding, explicit addition of artificial dissipation or through the use of stabilizers). However, unless carefully controlled, numerical dissipation can also overcome the SGS contribution thereby reducing the accuracy and predictive capability of the LES approach. Furthermore, as shown by Gresho and Lee [24], dissipative schemes do not provide any obvious warning of lack of resolution whereas this is usually quite clear with non-dissipative schemes due to the appearance of the so called “2-delta” waves. For these reasons, we strongly advocate the use of the non-dissipative schemes for these types of computations despite the increase in computational resources that usually accompanies the use of these schemes.

## LES OF TIP-CLEARANCE FLOW

The newly developed solver is used to analyze the three-dimensional flow structures in the tip-clearance region and the dynamic interactions of the tip-leakage vortex with the endwall turbulent boundary layer. The mesh size used for the present simulation is 449x351x129 ( $x \times y \times z$ ). The grid spacings based on the chord in the streamwise and transverse directions are in the ranges  $9.9 \times 10^{-4}$  -  $1.4 \times 10^{-2}$  and  $9.8 \times 10^{-4}$  -  $6.5 \times 10^{-3}$ , respectively and these grid spacings provide overall resolution of  $\Delta x^+ = 2.53$  - 35.84 and  $\Delta y^+ = 2.51$  - 16.64 based on the friction velocity at the inlet of the cascade. A total of 36 mesh points are allocated to the tip-gap region and this gives a normalized spanwise spacing of  $4.7 \times 10^{-3}$  and  $\Delta z^+ = 1.20$ . The remaining 96 spanwise points are distributed along the blade span by a hyperbolic tangent function. Prior to this simulation, coarser grid simulations had been carried out [18] to determine the resolution requirements and the final fine mesh was subsequently constructed using this information. The

simulation is advanced in time with maximum CFL number equal to 4 which corresponds to  $\Delta t \approx 0.73 \times 10^{-3}$ , and each time step requires a wallclock time of about 900 seconds when 32 CPU's of SGI Origin 3800 are used. The present results are obtained by integrating the solution over an interval of about  $11 C/U$ .

In the experiments [9, 10], hot wire measurements were made at four planes downstream of the blade trailing edge (two of which are shown in Fig. 7) in order to quantify the mean and turbulence characteristics of the endwall tip-leakage flow. In order to validate our LES computations we have made qualitative as well as quantitative comparisons with the experimental data on these planes.

Figure 8 shows a visualization of an averaged flowfield using the  $\Omega_2$ -vortex technique of Jeong and Hussain [25]. The averaging time is  $5 C/U$ , which although is not sufficient for full statistical convergence still gives us a reasonable view of the vortex topology associated with tip-leakage flow. The overall flow structures mainly consist of three distinct vortical regions. The vortical structures in A are generated near the leading edge and rotate in the direction opposite to the tip-leakage vortex B. Small scale vortical structures are abundant in the trailing edge endwall region and are generated by the interaction between the tip-separation vortices and the tip-leakage vortex from the neighboring blade. Similar observations have been reported by experiments [9, 10]. These complex vortical flows clearly affect the pressure distributions on both sides of rotor blade. As seen in Fig. 9, losses in pressure rise are noticeable near the endwall. The pressure distribution far from the endwall is generally comparable with that of experiment with stationary endwall [26] and indicates that the current mesh topology is capable of resolving the gross features of the blade boundary layer. Marginal grid resolution on the blade boundary layer, especially near leading and trailing edges may be responsible for the discrepancies observed in the pressure distribution in these regions.

The wake profiles, which are obtained at  $z/C_a = 0.9$  in the present LES and  $z/C_a = 1$  in the experiment with a stationary endwall [9], are plotted in Fig. 10 in terms of the mean streamwise velocity. Here  $C_a$  is the axial chord length by which the locations are normalized. These wake profiles and the velocity contours in the subsequent figures are normalized by the local maximum velocity in the plane to account for any mass leakage in the experiments [9, 10, 27]. As seen in Fig 10, the wake location is captured correctly by the LES in all the measurement planes. The wider wake predicted by LES, which is also evident in Figs. 11-14, may be the result of the spanwise ( $z$ ) domain size restriction or the grid resolution. Discrepancies in velocity magnitudes, particularly on the pressure side, are also observed in the three downstream locations.

Figures 11 and 12 represent the streamwise velocity contours from the present LES and experiment [10] at  $x/C_a = 1.51$  and  $x/C_a = 2.74$ , respectively, as seen by an observer looking upstream (see Fig. 7). Vertical bundles of the mean streamwise velocity contours are present in the wakes of rotor blades, and the tip-leakage vortices are found near the endwall in both the present LES and the experiment. Compared with

the experimental findings, the tip-leakage vortex predicted by the LES is reasonable in size and location. A closer examination of the results indicates that the small under-prediction in size may have been caused in part by the relatively small domain size in the spanwise direction.

The corresponding Reynolds stresses also appear reasonable relative to experimental measurements. As seen in Figs. 13 and 14, the tip-leakage vortex is the main source of turbulence generation in the downstream flowfield and results in low-pressure fluctuations near the endwall region. Figure 15 shows the instantaneous and time-averaged pressure contours in an  $x$ - $y$  plane very close to the moving endwall ( $z=0.008C_a$ ). The spatial variations of the negative pressure relative to the mean values appear to be highly correlated with the tip-leakage flow. These results indicate that a strong circular motion is developed by the tip-leakage vortex around the low-pressure core and this structure travels downstream expanding in size and generating intense fluctuations in the endwall region.

The energy spectra from the present LES and the experiment [10] in the tip-leakage region ( $x=1.51C_a$ ,  $y=1.4C_a$ ,  $z=0.1C_a$ ) are shown in Fig. 16. The spectra from both the LES and the experiment clearly show the presence of the inertial subrange. The spectral peaks suggest the presence of distinct coherent motions in the tip-leakage flow. It is also important to note that the present numerical scheme appears to be good in predicting the energies in a wide frequency range without excessive numerical dissipation.

## CONCLUSIONS

In order to analyze the temporal and spatial dynamics of the rotor tip-clearance flow and determine the underlying mechanism for the low-pressure fluctuations, a large-eddy simulation solver which combines an immersed-boundary technique with a generalized curvilinear structured grid has been developed. Numerical aspects related to the parallelization, the implementation of immersed boundary method and SGS model for fully inhomogeneous flow and grid skewness have been examined.

Results from the simulations show that the method is capable of capturing the complex flow features observed in well documented experiments. The flowfield is found to exhibit strong circular motions associated with the tip-leakage and tip-separation vortices. These vortical structures are found to convect downstream, expand in size and generate intense turbulent fluctuations in the endwall region. Qualitative and quantitative agreements with experiments in terms of velocity, Reynolds stresses and energy spectra have been observed in the downstream measurement locations. A detailed analysis of the data generated from these simulations should allow us to gain some insight into the spatio-temporal dynamics of the tip-clearance flow and mechanisms for cavitation-inducing low-pressure fluctuations. Results from this analysis will be presented in the future.

## ACKNOWLEDGMENTS

The authors acknowledge the support of the Office of Naval Research under Grant No. N00014-99-1-0389, with Drs. Patrick Purtell and Ki-Han Kim as program managers. Computer time was provided by a DoD Challenge Project Grant (C82) through ARL and ASC Major Shared Resource Centers. The authors would also like to thank Professor William Devenport of VPI for providing his experimental data.

## REFERENCES

- [1] Hoeger, M., Fritsch, G., and Bauer, D., 1999, "Numerical Simulation of the Shock-Tip Leakage Vortex Interaction in a HPC Front Stage," *ASME J. Turbomach.*, **121**, pp. 456-468.
- [2] Ameri, A. A., Steinthorsson, E., and Rigby, D. L., 1999, "Effects of Tip Clearance and Casing Recess on Heat Transfer and Stage Efficiency in Axial Turbines," *ASME J. Turbomach.*, **121**, pp. 683-693.
- [3] Wenger, C. W., Devenport, W. J., Wittmer, K. S., and Muthanna, C., 1998, "Two-Point Measurements in the Wake of a Compressor Cascade," *AIAA Paper 98-2556*.
- [4] Kameier, F., and Neise, W., 1997, "Experimental Study of Tip Clearance Losses and Noise in Axial Turbomachines and Their Reduction," *ASME J. Turbomach.*, **119**, pp. 460-471.
- [5] Zierke, W. C., Farrel, K. J., and Straka, W. A., 1995, "Measurement of the Tip Clearance Flow for a High-Reynolds-Number Axial-Flow Rotor," *ASME J. Turbomach.*, **119**, pp. 1-8.
- [6] Kang, S., and Hirsch, C., 1993, "Experimental Study on the Three-Dimensional Flow within a Compressor Cascade with Tip Clearance: Part I-Velocity and Pressure Fields, and Part II-The Tip Leakage Vortex," *ASME J. Turbomach.*, **115**, pp. 435-443.
- [7] Kang, S., and Hirsch, C., 1994, "Tip Leakage Flow in Linear Compressor Cascade," *ASME J. Turbomach.*, **116**, pp. 657-664.
- [8] Storer, J. A., and Cumpsty, N. A., 1990, "Tip Leakage Flows in Axial Compressors," *ASME Paper 90-GT-127*.
- [9] Muthanna, C., 1998, "Flowfield Downstream of a Compressor Cascade with Tip Leakage," MS Thesis, Department of Aerospace Engineering, Virginia Polytechnic Institute and State University.
- [10] Wang, Y., 2000, "Tip Leakage Flow Downstream of a Compressor Cascade with Moving End Wall," MS Thesis, Department of Aerospace Engineering, Virginia Polytechnic Institute and State University.
- [11] Choi, H., Moin, P., and Kim, J., 1992, "Turbulent Drag Reduction: Studies of Feedback Control and Flow over Riblets," Report TF-55, Department of Mechanical Engineering, Stanford University.
- [12] Beaudan, P., and Moin, P., 1994, "Numerical Experiments on the Flow Past a Circular Cylinder at Sub-Critical Reynolds Number," Report TF-62, Department of Mechanical Engineering, Stanford University.
- [13] Mittal, R., and Moin, P., 1997, "Suitability of Upwind-Biased Schemes for Large-Eddy Simulation of Turbulent Flows," *AIAA J.*, **36**, pp. 1415-1417.
- [14] Meneveau, C., Lund, T. S., and Cabot, W. H., 1996, "A Lagrangian Dynamic Subgrid-Scale Model of Turbulence," *J. Fluid Mech.*, **319**, pp. 233-242.
- [15] Germano, M., Piomelli, U., Moin, P., and Cabot, W. H., 1991, "A Dynamic Subgrid-Scale Eddy-Viscosity Model," *Phys. Fluids A3*, pp. 1760-1765.
- [16] Lund, T. S., Wu, X., and Squires, K. D., 1998, "Generation of Turbulent Inflow Data for Spatially-Developing Boundary Layer Simulations," *J. Comp. Phys.*, **140**, pp. 233-258.
- [17] Kunz, R. F., Lakshminarayana, B., and Basson, A. H., 1993, "Investigation of Tip Clearance Phenomena in an Axial Compressor Cascade Using Euler and Navier-Stokes Procedures," *ASME J. Turbomach.*, **115**, pp. 453-467.
- [18] You, D., Mittal, R., Wang, M., and Moin, P., 2002, "Large-Eddy Simulation of a Rotor Tip-Clearance Flow," *AIAA Paper 2002-0981*.
- [19] Thompson, J. F., Warsi, Z. U. A., and Mastin, C. W., 1985, *Numerical Grid Generation: Foundation and Applications*, North-Holland.
- [20] Fadlun, E. A., Verzicco, R., Orlandi, P., and Mohd-Yusof, J., 2000, "Combined Immersed-Boundary Finite-Difference methods for Three-Dimensional Complex Flow Simulations," *J. Comp. Phys.*, **161**, pp. 35-60.
- [21] Park, J., Kwon, K., and Choi, H., 1998, "Numerical Solutions of Flow Past a Circular Cylinder at Reynolds Numbers up to 160," *KSME Int. J.*, **12**, pp. 1200-1205.
- [22] Williamson, C. H. K., 1989, "Oblique and Parallel Modes of Vortex Shedding in the Wake of a Circular Cylinder at Low Reynolds Numbers," *J. Fluid Mech.*, **206**, pp. 579-627.
- [23] Mittal, R., Venkatasubramanian, S., and Najjar, F. M., 2001, "Large Eddy Simulation of Flow Through a Low-Pressure Turbine," *AIAA Paper 2001-2560*.
- [24] Gresho, P. M., and Lee, R. L., 1981, "Don't Suppress Wiggles - They're Telling You Something," *Computers & Fluids*, **9**, pp. 223-253.
- [25] Jeong, J., and Hussain, F., 1995, "On the Identification of a Vortex," *J. Fluid. Mech.*, **285**, pp. 69-94.
- [26] Muthanna, C., 2002, "The Effects of Free Stream Turbulence on the Flow Field through a Compressor Cascade," Ph.D. Thesis, Department of Aerospace Engineering, Virginia Polytechnic Institute and State University.
- [27] Khorrami, M. R., Li, F., and Choudhan, M., 2002, "Novel Approach for Reducing Rotor Tip-Clearance-Induced Noise in Turbofan Engines," *AIAA J.*, **40**, pp. 1518-1528.

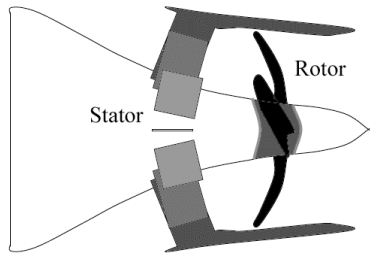


Figure 1: Example of a ducted propeller with tip-clearance.

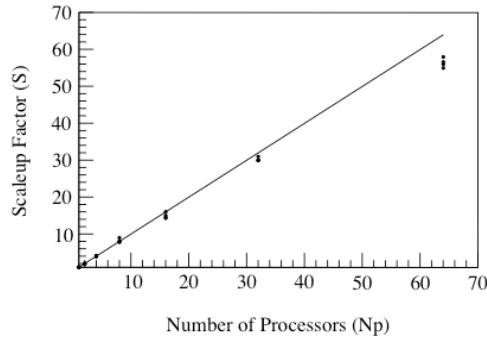


Figure 2: Parallel performance of the solver on a SGI Origin 2000 platform. The solid line represents linear scaleup and symbols represent actual scaleup.

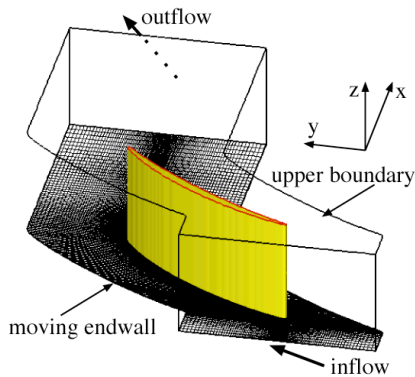


Figure 3: Flow configuration and coordinate system for LES of rotor tip-clearance flow.

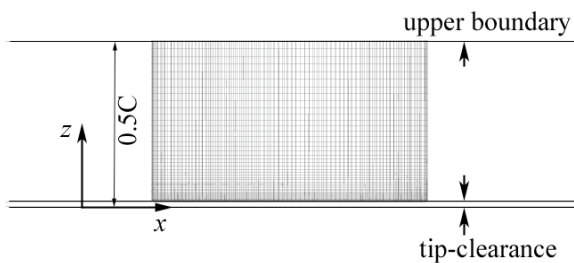
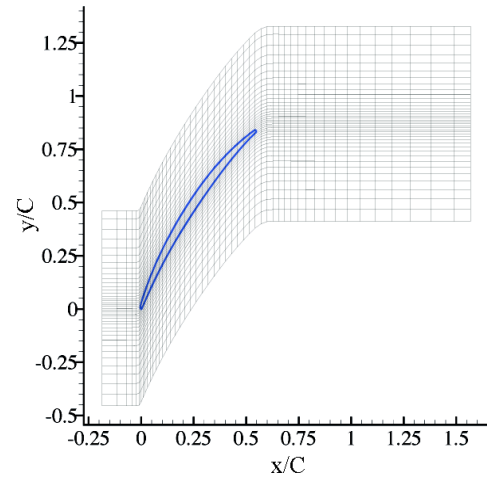
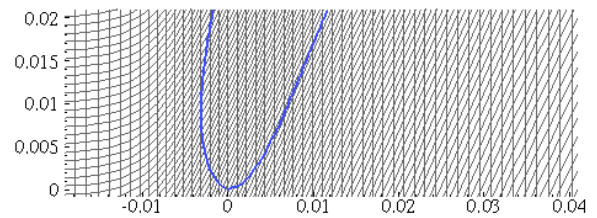


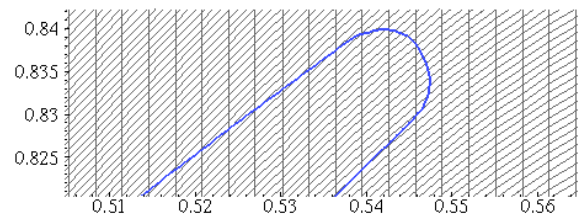
Figure 4: Computational domain and Cartesian mesh distribution on the blade in the  $x$ - $z$  direction (1/2 lines plotted).



(a)



(b)



(c)

Figure 5: (a) Full computational domain and curvilinear mesh in the  $x$ - $y$  plane used in conjunction with immersed boundary method for tip-clearance flow (1/6 lines plotted); (b) close-up view of the mesh near leading edge; (c) close-up view of the mesh near trailing edge.

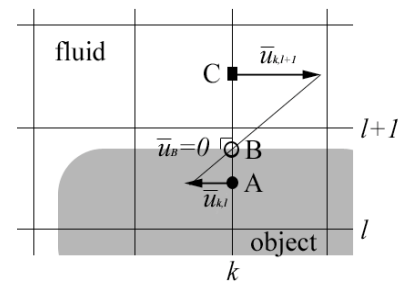


Figure 6: Example of body forcing in the immersed boundary. A body force is assigned to point A using velocity,  $\bar{u}_{k,l}$  which is extrapolated from the velocities at B ( $\bar{u}_B = 0$ ) and C ( $\bar{u}_{k,l+1}$ ).

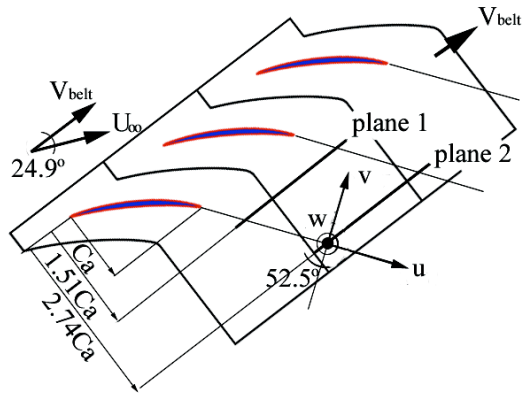


Figure 7: Measurement planes where comparisons are made between present LES and experiment [10]

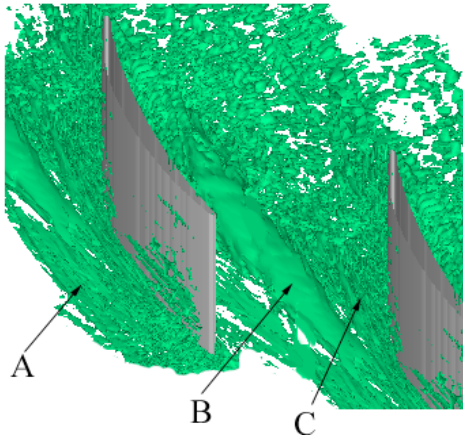


Figure 8:  $\lambda_2$  iso-surfaces from partially averaged flowfield. A, B and C represent distinct vortical regions.

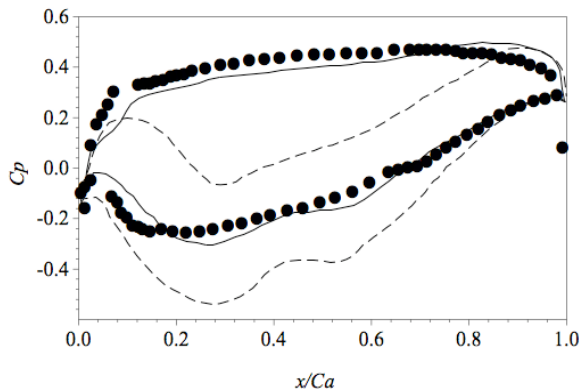


Figure 9: Pressure distributions on the blade surface. Upper and lower lines and circles are from suction and pressure surfaces, respectively. —, LES at  $z/C_a = 0.9$ ; ---, LES at  $z/C_a = 0.03$ ; ●, experiment [26] at  $z/C_a = 0.916$ .

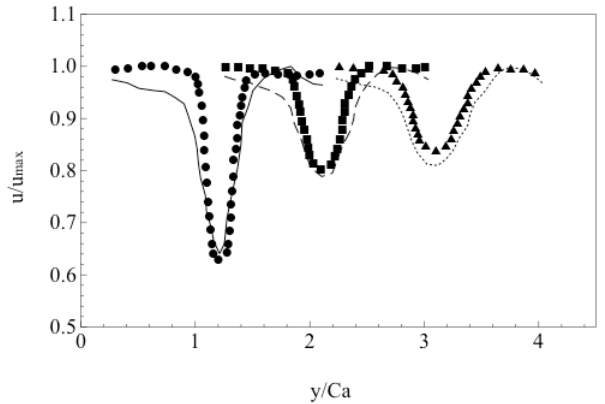


Figure 10: Mean velocity profiles in the rotor blade wake. Lines are from the present LES, and symbols are from the experiment [9]. —●—,  $x/C_a=1.366$ ; -■-,  $x/C_a=2.062$ ; ····▲····,  $x/C_a=2.74$ .

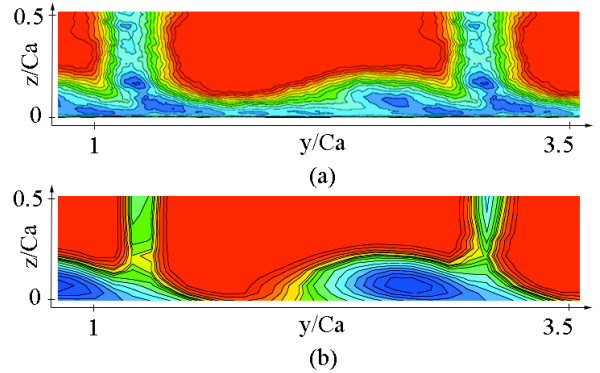


Figure 11: Contour plots of mean streamwise velocity normalized by the local maximum velocity at  $x/C_a=1.51$ . (a) present LES; (b) experiment [10]. Contour levels are from 0.5 to 1.0 by 0.02.

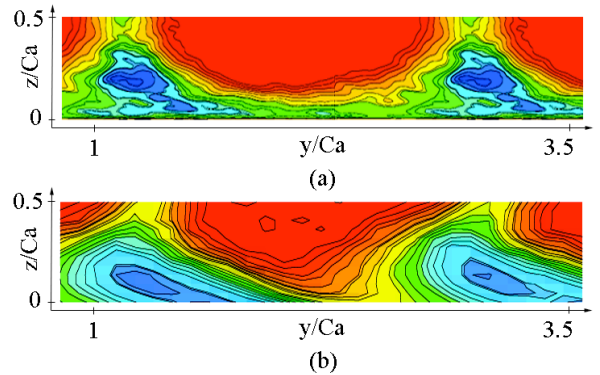


Figure 12: Contour plots of mean streamwise velocity normalized by the local maximum velocity at  $x/C_a=2.74$ . (a) present LES; (b) experiment [10]. Contour levels are from 0.6 to 1.0 by 0.2.



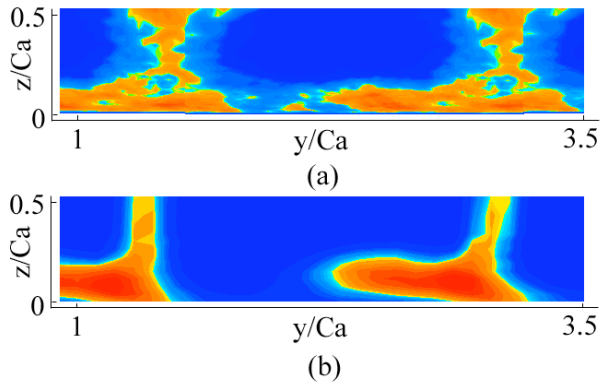


Figure 13: Contour plots of  $\overline{v|v|}$  at  $x/C_a=1.51$ . (a) present LES; (b) experiment [10]. Contour levels are from 0.001 to 0.01 by 0.0005.

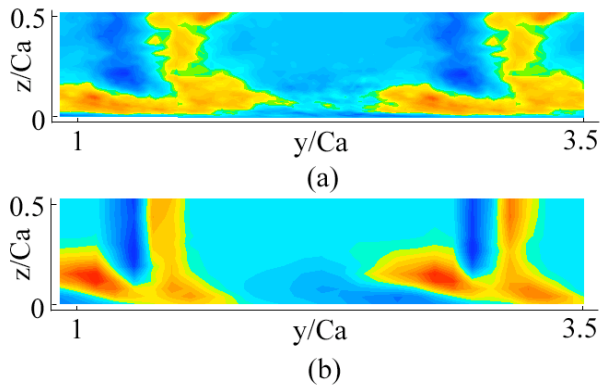


Figure 14: Contour plots of  $\overline{u|u|}$  at  $x/C_a=1.51$ . (a) present LES; (b) experiment [10]. Contour levels are from -0.003 to 0.003 by 0.0003.

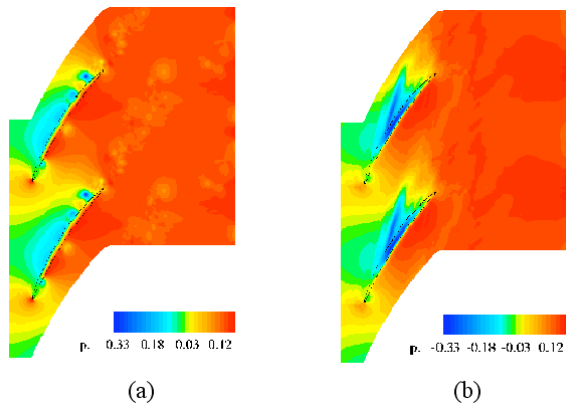
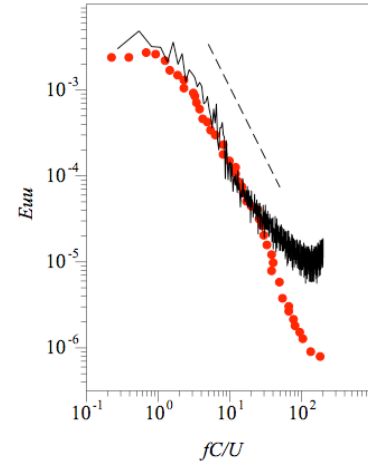
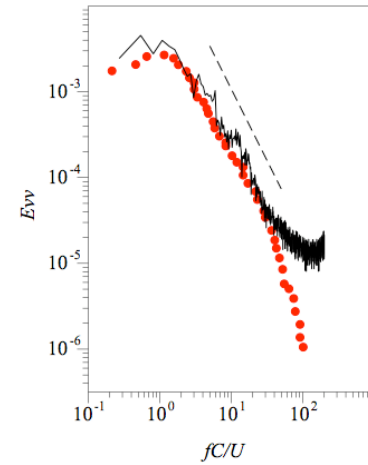


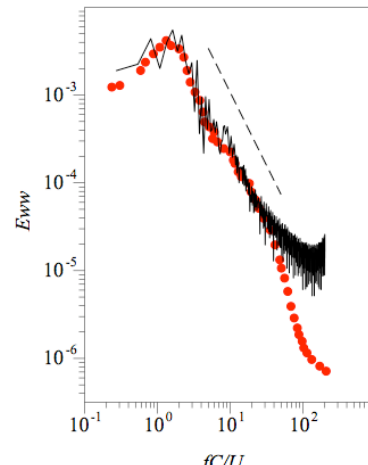
Figure 15: (a) Instantaneous and (b) time-averaged pressure contours in the tip-gap region ( $z/C_a = 0.008$ ).



(a)



(b)



(c)

Figure 16: Energy spectra as a function of frequency in the tip-leakage region at  $x/C_a=1.51$ ,  $y/C_a=1.4$ ,  $z/C_a=0.1$ . (a)  $E_{uu}$ ; (b)  $E_{vv}$ ; (c)  $E_{vwv}$ . Solid lines are from the present LES, symbols are from the experiment [10] and dashed lines are of  $-5/3$  slope.